ROYAL SOCIETY OF CHEMISTRY

PAPER

Check for updates

Dual-carbon coupling modulated bimetallic sulfides as high-efficiency bifunctional oxygen electrocatalysts in a rechargeable Zn–air battery†

Yongxia Wang,[*ab] Jingjing Liu,[a] Jiaxi Liu,[a] Zhaodi Wang,[a] Biyan Zhuang,[a] Nengneng Xu,[a] Xiangzhi Cui [ID] [*bd] and Jinli Qiao[*ac]

The design and construction of high-efficiency carbon based non-precious metal electrocatalysts for oxygen reduction and oxygen evolution reactions (ORR and OER) with sluggish kinetics are of great importance but remain a big challenge. In this work, a 3D hybrid of bimetallic (Co/Fe) sulfide nanoparticles anchored on nitrogen-doped graphene and CNTs ($Co_{0.2}Fe_{0.6}S_x$-Gra/CNT) is fabricated *via* a ball-milling assisted *in situ* pyrolysis process. Benefitting from the synergetic effects between the carbon matrix and metallic sulfides, the optimized $Co_{0.2}Fe_{0.6}S_x$-Gra/CNT hybrid exhibits a high half-wave voltage up to 0.822 V for the ORR and a low overpotential of 540 mV at 10 mA cm^{-2} for the OER, outperforming $Co_{0.2}Fe_{0.6}S_x$-Gra and even a commercial Pt/C catalyst. Meanwhile, a home-made Zn–air battery with the hybrid as a cathode catalyst delivers a maximum power density up to 366 mW cm^{-2}, along with a long-term charge and discharge stability at 10 mA cm^{-2}. The excellent performances of the hybrid toward the ORR and OER are mainly attributed to the plentiful electron transfer channels provided by the 3D intertwined carbon matrix and enriched active sites derived from a dual-carbon coupling enhancement effect, which induce a change in the electronic structure and increase in the electron cloud density of the bimetallic sulfides and nitrogen dopant configuration. This work proves the importance of a carbon support to enhance the catalytic performance of non-precious metal-based catalysts and provides possibility of metal sulfides as bifunctional catalysts for the ORR/OER in a rechargeable Zn–air battery.

Introduction

With the increasing environmental problems and demand for sustainable energy, renewable and green energy sources have received much attention and rapid development in the past few decades. Among them, metal–air batteries have become a rising hotspot of research studies because of their advantages of ultra-high energy density, environmental friendliness, and other properties.[1–3] However, the overall efficiency of a rechargeable battery remains a great challenge owing to the sluggish kinetics at the oxygen electrode, known as the oxygen reduction reaction

(ORR) and oxygen evolution reaction (OER). To date, the best-performing electrocatalysts remain dominated by precious metals (Pt, Ir, Ru, *etc.*),[4,5] which suffer from high cost, scarcity and unstable catalytic performance, which limit their widespread application. Numerous endeavors have been devoted to the exploration and construction of economical, high-efficiency and robust bifunctional oxygen electrocatalysts.[6,7] Transition-metal compounds, including oxides,[7,8] nitrides,[9,10] phosphides[11,12] and sulfides,[13,14] have attracted considerable attention owing to their unique physicochemical properties.

Among the various transition-metal compounds, cobalt sulfides show great potential in rechargeable Zn–air batteries owing to their natural abundance, chemical stability and efficient activity.[15–18] Co_9S_8 has been reported as an electrocatalyst for the ORR *via* experiments combined with theoretical study.[19] $Ni_3S_4@CoS_x$-NF has also been successfully obtained and exhibits bifunctional oxygen electrocatalytic activity.[20] Unfortunately, however, the poor electronic conductivity and severe aggregation seriously limit their catalytic performance.[21,22] Carbon-based supports play an important role in enhancing the stability of the catalysts owing to the advantages of excellent electronic conductivity, high structural stability and resistance to acid and base electrolytes.[23] Two-dimensional (2D) planar

aState Key Laboratory for Modification of Chemical Fibers and Polymer Materials, College of Environmental Science and Engineering, Donghua University, 2999 Ren'min North Road, Shanghai 201620, China. E-mail: wyx912@dhu.edu.cn

bState Key Laboratory of High Performance Ceramics and Superfine Microstructure, Shanghai Institute of Ceramics, Chinese Academy of Sciences, Shanghai 200050, China

cShanghai Institute of Pollution Control and Ecological Security, 1515 North Zhongshan Road, Shanghai 200092, China

dSchool of Chemistry and Materials Science, Hangzhou Institute for Advanced Study, University of Chinese Academy of Sciences, Hangzhou 310024, P.R. China

† Electronic supplementary information (ESI) available. See DOI: https://doi.org/10.1039/d4se00793j

graphene and one-dimensional (1D) carbon nanotubes (CNTs) with large specific surface area and excellent conductivity have been explored as key supports for oxygen electrocatalysts.[13,24,25] For example, $Co_{1-x}S$ loaded on graphene was reported to exhibit an ORR current density of 1.1 mA cm^{-2} at a voltage of 0.7 V (vs. RHE).[26] Meanwhile, homogeneous $NiCo_2S_4$ anchored on N-doped CNT demonstrates bifunctional activities for ORR and OER, which are mainly attributed to the coupling interaction between the $NiCo_2S_4$ particles and CNT supports, leading to the altered electronic structure and enriched electron transfer pathway.[27] Moreover, the synergistic effects between the metallic sulfide nanoparticles and carbon support have also been reported.[28] However, not much work has been done to study the role of carbon support on the microstructure and electrocatalytic performance of the metallic sulfides as far as we know. Factually, much more efforts should be made toward revealing the influence and function of different types and dimension of carbon support on the metallic sulfide-based bifunctional catalysts for ORR and OER.

Herein, we present a facile and efficient route to fabricate a hybrid of Co/Fe bimetallic sulfide nanoparticles anchored on nitrogen-doped graphene and CNT ($Co_{0.2}Fe_{0.6}S_x$-Gra/CNT) via ball-milling assisted in situ pyrolysis process. Metallic sulfides and nitrogen dopants are uniformly distributed on the graphene/CNT matrix. The hybrid ($Co_{0.2}Fe_{0.6}S_x$-Gra/CNT) demonstrates excellent electrocatalytic activities for ORR and OER, with a half-wave voltage of 0.822 V (vs. RHE) for ORR and voltage of 1.77 V at 10 mA cm^{-2} for OER in 0.1 M KOH electrolytes, outperforming the single-graphene network ($Co_{0.2}Fe_{0.6}S_x$-Gra), even the commercial Pt/C catalyst. Moreover, the home-made Zn–air battery with the $Co_{0.2}Fe_{0.6}S_x$-Gra/CNT as a cathode catalyst delivers a maximum power density up to 366 mW cm^{-2}, along with a long-term charge–discharge stability at the current of 10 mA cm^{-2}. The boosting catalytic activity and stability of the bifunctional catalyst for ORR and OER are mainly attributed to the abundant electron transfer channels provided by the 3D intertwined carbon matrix and enriched active sites derived from the dual-carbon synergistic enhancement effect-induced change of the electronic structure and increase of the electron cloud density of the bimetallic sulfides and nitrogen dopant configuration. This work further proves the important role of the carbon support on the enhancement of the catalytic performance of the metallic sulfide catalyst and provides the possibility of metallic sulfides as bifunctional catalysts for the ORR/OER in the rechargeable Zn–air battery.

Results and discussion

The hybrid of Co/Fe sulfide nanoparticles anchored on nitrogen-doped graphene and CNTs ($Co_{0.2}Fe_{0.6}S_x$-Gra/CNT) is successfully fabricated via ball-milling assisted in situ pyrolysis process, as schematically illustrated in Fig. 1a. On the one side, the precursors of metal salts, thiourea, graphene and CNT were mixed more evenly during the mechanical ball-milling process. On the other side, a large number of structural defects in graphene and CNT can be manufactured due to the cleavage of C–C bonds via the strong mechanical shear forces.[29,30] Thus, the
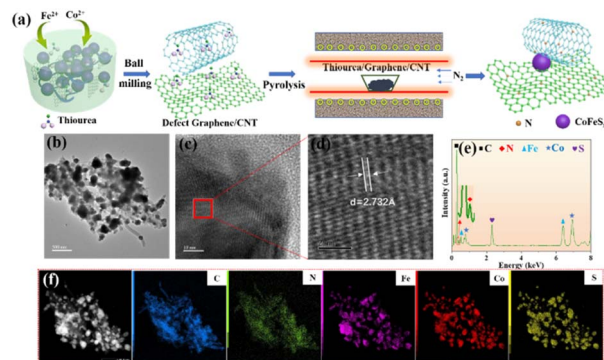

Fig. 1 (a) Schematic illustration of the synthesis of CoFeS$_x$-Gra/CNT; (b) TEM (c and d) HRTEM images and (e) EDS of Co$_{0.2}$Fe$_{0.6}$S$_x$-Gra/CNT; (f) element mappings of the NSP-Gra.

heteroatoms of nitrogen and sulfur decomposed from thiourea are in situ doped into the graphene and CNT matrix during the pyrolysis process. Meanwhile, the metal sulfide nanoparticles derived from the metal salts and thiourea are uniformly dispersed on the carbon matrix. For comparison, the hybrid of metal sulfides anchored on graphene ($Co_{0.2}Fe_{0.6}S_x$-Gra) was also fabricated via the similar synthesis process.

The micro-morphology of the obtained $Co_{0.2}Fe_{0.6}S_x$-Gra/CNT hybrid was observed and analyzed using TEM. As demonstrated in Fig. 1b, graphene and CNT are intertwined with each other, and the successful fabrication of the intertwined dual-carbon network favors the enhanced electrocatalytic properties of ORR and OER. The metal sulfide nanoparticles are observed to be dispersed in an orderly manner on the graphene and CNT matrix. From the HRTEM morphologies given in Fig. 1c and d, the hybrid shows the lattice fringes with a spacing of 2.732 Å corresponding to the (422) plane of Co_8FeS_8, indicating the formation of metal sulfides. EDS in Fig. 1e demonstrates the strong signals of C, Co, Fe, S and N, confirming the formation of $Co_{0.2}Fe_{0.6}S_x$-Gra/CNT. Moreover, the Co, Fe, S and N are dispersed evenly on the carbon matrix, according to the homogeneous elemental mappings in Fig. 1f. Moreover, the dispersion of Co, Fe and S illustrate a perfect overlap, consolidating the successful fabrication of the metal sulfides.

The microstructure and phase composition of the hybrids of $Co_{0.2}Fe_{0.6}S_x$-Gra/CNT and $Co_{0.2}Fe_{0.6}S_x$-Gra are determined via the XRD and Raman spectra. From the XRD spectra in Fig. 2a, an obvious diffraction peak can be observed at 26°, belonging to the [002] peak of the graphite structure (PDF 41-1487). For $Co_{0.2}Fe_{0.6}S_x$-Gra/CNT, the diffraction peaks are mainly a to Co_8FeS_8 (PDF 29-0484). The peaks of $Co_{0.2}Fe_{0.6}S_x$-Gra are relatively complex, corresponding to the $Co_{1-x}S$ (PDF 42-0826) and FeS (PDF 15-0037), aside from the main Co_8FeS_8. Combining the above analysis, the metal sulfide in the $Co_{0.2}Fe_{0.6}S_x$-Gra/CNT hybrid exhibits a pure phase structure of Co_8FeS_8, suggesting that the introduction of CNT is favorable for the formation of bimetallic sulfide. Raman spectra can further determine the structural characteristic of the hybrids, which demonstrate two typical peaks at 1350 and 1580 cm^{-1} as shown in Fig. 2b, corresponding to the D and G bands, respectively. The I_D/I_G ratio is
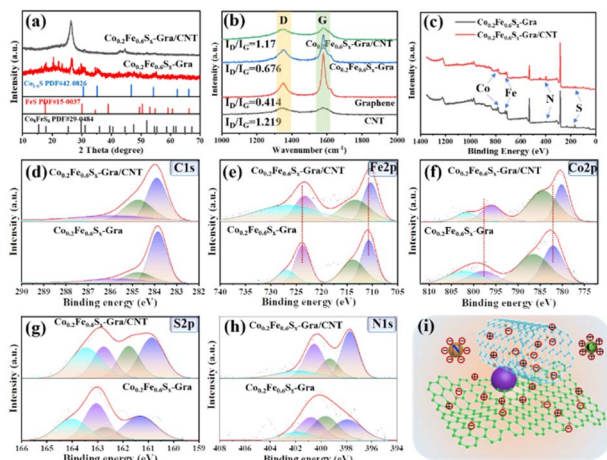
Fig. 2 XRD (a), Raman spectra (b) and XPS spectra (c) of $Co_{0.2}Fe_{0.6}S_x$-Gra/CNT; XPS spectra of C 1s (d), Fe 2p (e), Co 2p (f), S 2p (g), and N 1s (h). (i) The electronic structure schematic illustration of $Co_{0.2}Fe_{0.6}S_x$-Gra/CNT.

an important index to reflect the disorder degree of carbon.[31] The calculated I_D/I_G ratio of the initial graphene and CNT are 0.414 and 1.219, respectively, demonstrating a distinct degree of disorder. Such an obvious microstructural difference affects the formation and growth of the metallic sulfides to a certain degree. The obtained hybrids of $Co_{0.2}Fe_{0.6}S_x$-Gra/CNT and $Co_{0.2}Fe_{0.6}S_x$-Gra demonstrate the similar I_D/I_G ratio of 1.17, a value between graphene and CNT indicating the disorder degree between the two. The results from both XRD and Raman provide favorable evidence of the co-effect of graphene and CNT on the formation of Co_8FeS_8 nanoparticles.

The components and chemical states of the obtained hybrids of $Co_{0.2}Fe_{0.6}S_x$-Gra/CNT and $Co_{0.2}Fe_{0.6}S_x$-Gra are determined by XPS. From the survey XPS spectra in Fig. 2c, the obvious peaks at the binding energies of 284.8, 712.3, 782.4, 398.1 and 182.6 eV can be assigned to C 1s, Fe 2p, Co 2p, N 1s and S 2p, respectively, indicating that the target elements can be readily anchored and/or doped into the carbon matrix by the *in situ* pyrolysis strategy assisted with wet ball-milling process. The chemical valence states of the C, Fe, Co, N and S are studied to gain more insight into the structural information of the hybrids, and the XPS patterns of all elements are fitted *via* Gaussian fitting method. From the C 1s spectra in Fig. 2d, three main peaks at binding energies of 283.8, 284.7 and 285.9 eV belong to C–C, C–N and C–N,[32] respectively, indicating the successful doping of the nitrogen atom into the carbon matrix. Fig. 2e gives the Fe 2p spectra, from which the four peaks fitted at 710.2, 713.2, 723.2 and 726.6 eV belong to Fe^{2+} $2p_{3/2}$, Fe^{3+} $2p_{3/2}$, Fe^{2+} $2p_{1/2}$ and Fe^{3+} $2p_{1/2}$, respectively.[33,34] It is worth noting that the Fe peaks of $Co_{0.2}Fe_{0.6}S_x$-Gra/CNT move to relatively low binding energy positions, compared with those of $Co_{0.2}Fe_{0.6}S_x$-Gra at 710.6, 713.7, 723.7 and 726.8 eV, respectively. Furthermore, the Co peaks shift to the low binding energy, as shown in Fig. 2f. Specifically, the peaks of Co^{3+} $2p_{3/2}$, Fe^{2+} $2p_{3/2}$, Fe^{3+} $2p_{1/2}$ and Fe^{2+} $2p_{1/2}$ for $Co_{0.2}Fe_{0.6}S_x$-Gra/CNT are at binding energies of 780.1, 784.2, 785.8 and 801.5 eV, lowering than those of

$Co_{0.2}Fe_{0.6}S_x$-Gra at 781.9, 786.4, 797.8 and 802.1 eV, respectively. The obvious peak position shifts to low binding energy indicates the enhancement of the force between the Fe and Co species, which may be also favorable to promote the electrocatalytic performance for the bifunctional oxygen reaction. More importantly, it confirms the change of the electronic structure and an increase of the electron cloud density of the bimetallic sulfide species in the $Co_{0.2}Fe_{0.6}S_x$-Gra/CNT hybrid, endowing the hybrid with an enhanced electrocatalytic activity.[35,36] Similar to the above phenomena, the fitted S 2s peaks of $Co_{0.2}Fe_{0.6}S_x$-Gra/CNT move to the lower binding energy, given in Fig. 2g. Nitrogen as a heteroatom doped in the carbon matrix, and structural forms are also fitted and analyzed, as listed in Fig. 2h. Four typical configurations of nitrogen dopants in the carbon matrix are pyridinic-N, pyrrolic-N, graphitic-N and oxidized-N at binding energies of 398.1, 399.3, 400.7 and 401.9 eV, respectively.[37] Among them, the pyridinic-N, pyrrolic-N and graphitic-N have been deemed to play important roles in the electrocatalytic process of ORR and OER.[38,39] The contents of the different nitrogen configurations of the two hybrids are listed in Table 1, and there is an obvious difference of the third types of nitrogen configuration. According to most of the current reports, the pyridinic-N and graphitic-N species are more conducive to the ORR and OER.[40,41] The increased content of the pyridinic-N and graphitic-N suggest a better catalytic performance of $Co_{0.2}Fe_{0.6}S_x$-Gra/CNT.

The potential electronic structure of the $Co_{0.2}Fe_{0.6}S_x$-Gra/CNT hybrid is drawn in Fig. 2i. The heteroatom dopant can modify the carbon networks to induce the special surface chemical properties and electronic structures.[42] Especially, the heteroatoms with different electronegativity and electron spin density can induce synergetic effects among the different active species. For $Co_{0.2}Fe_{0.6}S_x$-Gra/CNT, the N doping with a larger electronegativity (3.04) than that of C atoms (2.55) render the adjacent C atoms as positively charged.[43] Additionally, the metallic sulfide composed of two metal elements demonstrates a markedly different electronic structure, in comparison with that of the monometallic sulfide.[37,44] More importantly, the obtained bimetallic sulfide (Co_8FeS_8) shows closely combined forces between Co and Fe induced by the synergistic effect of dual-carbon matrixes (graphene and CNT). Combined the above results and analysis, the unique microstructure and atomic configuration endow the $Co_{0.2}Fe_{0.6}S_x$-Gra/CNT hybrid with special advantages for electrochemical reaction.

The electrocatalytic performance of the fabricated hybrids of metal sulfides anchored on nitrogen-doped carbon for ORR are evaluated *via* the RDE and RRDE in the O_2-saturated alkaline

Table 1 The configurations of nitrogen dopants in $Co_{0.2}Fe_{0.6}S_x$-Gra and $Co_{0.2}Fe_{0.6}S_x$-Gra/CNT

| Nitrogen configuration	$Co_{0.2}Fe_{0.6}S_x$-Gra	$Co_{0.2}Fe_{0.6}S_x$-Gra/CNT
Pyridinic-N (%)	34.1	37.6
Pyrrolic-N (%)	24.0	16.9
Graphitic-N (%)	20.7	31.2
Oxidized-N (%)	21.2	14.2

solution (0.1 M KOH). The cycle voltammogram (CV) curves of the catalysts are plotted in Fig. 3a, from which it can be clearly seen that both $Co_{0.2}Fe_{0.6}S_x$-Gra/CNT and $Co_{0.2}Fe_{0.6}S_x$-Gra exhibit obvious oxygen reduction peaks, indicating the catalytic activity toward ORR. It is worth noting that the peak shifts from 0.71 V ($Co_{0.2}Fe_{0.6}S_x$-Gra) to a more positive potential of 0.78 V ($Co_{0.2}Fe_{0.6}S_x$-Gra/CNT) and increase in peak intensity, indicating a much higher ORR catalytic activity of the latter. From the linear scan voltammogram (LSV) curves in Fig. 3b, both the onset potential ($E_{onset} = 0.976$ V) and half-wave potential ($E_{1/2} = 0.822$ V) of $Co_{0.2}Fe_{0.6}S_x$-Gra/CNT are much higher than those of $Co_{0.2}Fe_{0.6}S_x$-Gra ($E_{onset} = 0.931$ V, $E_{1/2} = 0.782$ V) and the other reported carbon catalysts (Table S1†). The Tafel slope is considered as an important indictor to evaluate the kinetics process of ORR, and the corresponding values according to LSV curves are given in Fig. 3c. $Co_{0.2}Fe_{0.6}S_x$-Gra/CNT (99.4 mV dec^{-1}) exhibits a similar Tafel slope to Pt/C (97.8 mV dec^{-1}), and $Co_{0.2}Fe_{0.6}S_x$-Gra shows the highest Tafel slope up to 135.6 mV dec^{-1}, indicating the fast ORR kinetics for the obtained $Co_{0.2}Fe_{0.6}S_x$-Gra/CNT.

The H_2O_2 yield rate (H_2O_2%) and electron transfer number (n) of the $Co_{0.2}Fe_{0.6}S_x$-Gra/CNT were calculated based on disk and ring currents. As shown in Fig. 3d, the H_2O_2 yield rate is extremely low, and the value of n is close to 4 in the tested voltage range, indicating the 4e transfer process of $Co_{0.2}Fe_{0.6}S_x$-Gra/CNT with excellent ORR catalytic performance. Additionally, according to the Koutecky–Levich equations given in ESI† and the LSV curves at different rotation rates from 400 to 2025 rpm (Fig. S1a†), the Koutecky–Levich plots (Fig. S1b†) show the n of 3.95, further confirming the 4e transfer process of $Co_{0.2}Fe_{0.6}S_x$-Gra/CNT. The electrochemical double layer capacitance (C_{dl}) is linearly proportional to the electrochemical active surface area (ECSA), which can usually be used to reflect the catalytic performance of the catalyst.[45] The C_{dl} plotted in Fig. 3e is determined by CV curves at sweeping rates from 40 to 200 mV s^{-1} (Fig. S2 and S3†). The C_{dl} value of $Co_{0.2}Fe_{0.6}S_x$-Gra/CNT is

nearly twice that of $Co_{0.2}Fe_{0.6}S_x$-Gra, meaning there is a much higher ECSA of the former resulting from the dual-carbon network of graphene and CNT to provide abundant active sites. The higher ORR performance of $Co_{0.2}Fe_{0.6}S_x$-Gra/CNT is also connected to its lower charge transfer resistance (44 Ω) compared to that of $Co_{0.2}Fe_{0.6}S_x$-Gra (52 Ω), according to the electrochemical impedance spectroscopy (EIS) and the corresponding Nyquist plot (Fig. 3f), implying a fast electron transfer in $Co_{0.2}Fe_{0.6}S_x$-Gra/CNT during the ORR process. The unique network constructed by the 2D graphene plane and 1D CNT facilitates the exposure of active sites, provides a fast electron transfer channel, and then boosts the catalytic process.

Besides the catalytic performance for ORR, the properties of the obtained bifunctional catalyst for OER are also determined by RRDE. From Fig. 4a, the obtained hybrids exhibit much higher OER performance than the commercial Pt/C with a relatively smaller overpotential at the current density of 10 mA cm^{-2}. $Co_{0.2}Fe_{0.6}S_x$-Gra/CNT shows a slightly lower potential at 10 mA cm^{-2} than $Co_{0.2}Fe_{0.6}S_x$-Gra, indicating the slightly higher OER catalytic activity of the former. Similar to the trend of the LSV curves of OER, the Tafel slopes of the hybrids are lower than that of Pt/C (Fig. 4b), and the $Co_{0.2}Fe_{0.6}S_x$-Gra/CNT demonstrates the lowest Tafel slope indicating the fastest OER kinetics. To evaluate the overall oxygen electrode activity of the $Co_{0.2}Fe_{0.6}S_x$-Gra/CNT, the overvoltage (ΔE) between ORR and OER is given in Fig. 4c. The ΔE as the difference between $E_{1/2}$ for ORR and potential at 10 mA cm^{-2} for OER is calculated, and $Co_{0.2}Fe_{0.6}S_x$-Gra/CNT has a much smaller value of 0.943 V, outperforming that of Pt/C (1.014 V). Furthermore, the potential of the $Co_{0.2}Fe_{0.6}S_x$-Gra/CNT catalyst after 3000 cycles is about 1.802 V at 10 mA cm^{-2}, along with a small positive shift of 32 mV compared to the initial value (Fig. 4d), indicating the excellent catalytic stability for OER.

Combined with the results and analysis of $Co_{0.2}Fe_{0.6}S_x$-Gra/CNT as a bifunctional catalyst for ORR and OER, the potential catalytic mechanism is shown in Fig. 4e. The enhanced catalytic performance can be attributed to the following aspects: (1)
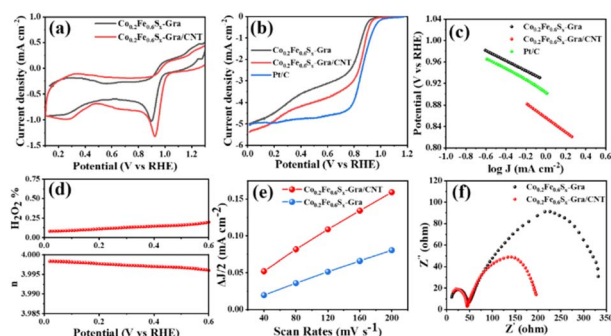
Fig. 3 (a) CV curves of the $Co_{0.2}Fe_{0.6}S_x$-Gra/CNT and 20% Pt/C at O_2-saturated 0.1 M KOH, with a loading of 200 μg cm^{-2} and scanning rate of 5 mV s^{-1}. (b) LSV curves of the catalysts at a scanning rate of 5 mV s^{-1} and rotation rate of 1600 rpm. (c) Tafel plots of the catalysts for the ORR. (d) Electron transfer number and H_2O_2 yield rate of $Co_{0.2}Fe_{0.6}S_x$-Gra/CNT. (e) The linear fitting plots of scan rates with capacitive current densities for $Co_{0.2}Fe_{0.6}S_x$-Gra and $Co_{0.2}Fe_{0.6}S_x$-Gra/CNT. (f) Nyquist plots of $Co_{0.2}Fe_{0.6}S_x$-Gra and $Co_{0.2}Fe_{0.6}S_x$-Gra/CNT.
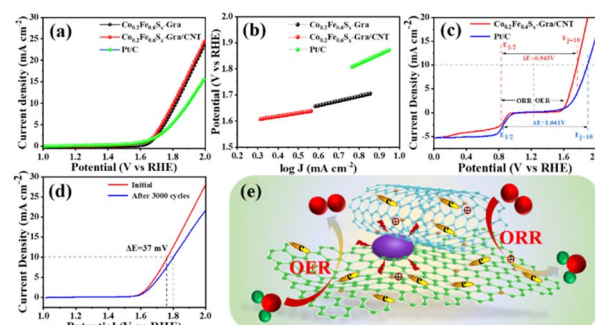
Fig. 4 (a) LSV curves of the catalysts for the OER in 0.1 M KOH with a scanning rate of 5 mV s^{-1} and rotating rate of 1600 rpm. (b) Tafel plots of the catalysts for OER. (c) Overall LSV curves of the catalysts at the rotating rate of 1600 rpm. (d) LSV curves of the $Co_{0.2}Fe_{0.6}S_x$-Gra/CNT for the OER before and after 3000 cycles. (e) The interaction schematic illustration of the metal sulfides and heteroatoms-doped graphene and CNTs for the ORR and OER processes.

heteroatoms doping. The dopants of N can induce rearrangement of the electron distribution in the carbon matrix.[46] The larger electronegativity of the N atom endows the adjacent C in graphene and CNT matrix with the positive characteristic, reducing the adsorb energy barrier of the O_2 molecules, thus accelerating the adsorption of O_2 and boosting the ORR catalytic activity.[47,48] (2) Nitrogen configuration. The pyridinic-N and graphitic-N have been considered as effective active species for ORR and OER. The pyridinic-N and graphitic-N are the main nitrogen species in $Co_{0.2}Fe_{0.6}S_x$-Gra/CNT, which is favorable for the high catalytic performance for ORR and OER. (3) Metallic sulfide microstructure. The Fe 2p and Co 2p XPS spectra confirm that the obtained bimetallic sulfide demonstrates closely combined forces between Co and Fe, a change of the electronic structure and an increased electron cloud density, endowing the catalyst with special catalytic performance. Additionally, the bimetallic materials present higher conductivity and larger active areas due to the synergistic effect of different metal elements, contrasting with their monometallic counterparts.[49–51] (4) Synergistic effect of the dual-carbon network. The 2D graphene planar and 1D CNT with the feature of excellent conductivity and large specific surface area provide fast electron and charge transfer pathway, greatly promoting the catalytic reaction. More importantly, the unique dual-carbon network can change the microstructure of the metallic sulfides and local configuration of the nitrogen dopant, promoting the formation of the catalytic active species for ORR and OER. Benefiting from the synergistic effect of the dual-carbon associated increased number of catalytic active sites, the $Co_{0.2}Fe_{0.6}S_x$-Gra/CNT demonstrates an intrinsically enhanced bifunctional electrocatalytic performance for ORR and OER.

The practical application of the obtained $Co_{0.2}Fe_{0.6}S_x$-Gra/CNT hybrid as a cathode catalyst is further evaluated in a system of the home-made rechargeable Zn–air battery, as shown in Fig. 5a. The carbon paper-loaded catalyst as an air electrode, and the charge–discharge properties are evaluated in 6 M KOH electrolyte at room temperature. Fig. 5b gives the polarization and power density curves, from which it can be seen that the open voltage is about 1.25 V. Delightfully, the Zn–air battery equipped with the fabricated $Co_{0.2}Fe_{0.6}S_x$-Gra/CNT demonstrates a high power density up to 366 mW cm^{-2}, outperforming the state-of-the-art carbon-based metal sulfide catalysts (Fig. 5c), including (Ni, Co)S$_2$ (152.7 mW cm^{-2}),[49] CuCo$_2$S$_4$ NSs@N-CNFs (232 mW cm^{-2}),[14] CoNiFe–S MNs (140 mW cm^{-2}),[52] CuCoS-4/N-rGO (143.2 mW cm^{-2}),[53] Co$_{9-x}$Ni$_x$S$_8$/NC (76 mW cm^{-2}),[54] Ni–Co–S@G/NSCT (171.2 mW cm^{-2}),[55] Ni–Fe–S/3NCQDs (94 mW cm^{-2}),[56] Co–Ni–S@NSPC (100 mW cm^{-2}),[57] NiCo$_2$S$_4$/N-CNT (147 mW cm^{-2}),[27] and NiS$_2$/CoS$_2$ (101 mW cm^{-2}).[21] Moreover, the home-made Zn–air battery exhibits excellent charge–discharge stability at a high current density of 10 mA cm^{-2} (shown in Fig. 5d), as investigated *via* a LAND test system, which shows a low voltage gap of 0.762 V after the 70 h charge and discharge cycles. Meanwhile, according to the charging test given in Fig. 5e, the battery demonstrates a stable charge potential of 1.25 V for 40 h. The outstanding charge and discharge performance confirms that the fabricated
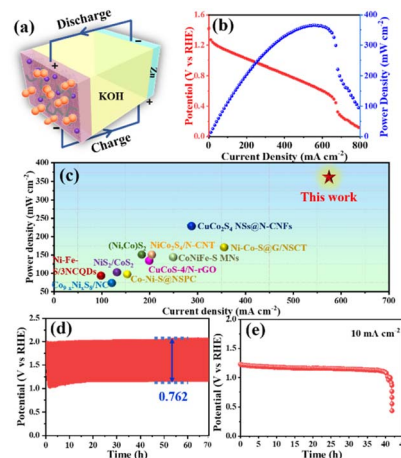

Fig. 5 (a) A home-made rechargeable Zn–air battery scheme with 6 M KOH as the electrolyte. (b) The polarization plots and power density curves of the Zn–air battery with $Co_{0.2}Fe_{0.6}S_x$-Gra/CNT as the air cathode. (c) The comparisons of power densities and current densities between the home-made Zn–air battery equipped with $Co_{0.2}Fe_{0.6}S_x$-Gra/CNT and the reported ones. (d) The discharge/charge cycling curves of rechargeable Zn–air batteries at 10 mA cm^{-2}. (e) The discharge curve of the home-made Zn–air battery at 10 mA cm^{-2}.

$Co_{0.2}Fe_{0.6}S_x$-Gra/CNT can be used as potential bifunctional catalysts with high catalytic activity and durability for ORR and OER in a practical rechargeable Zn–air battery.

We have developed a facile and effective approach to fabricate a hybrid with Co/Fe sulfide nanoparticles anchored on nitrogen-doped graphene and CNT ($Co_{0.2}Fe_{0.6}S_x$-Gra/CNT), along with uniformly dispersed nitrogen dopants with the feature of a relatively high ratio of pyrrolic-N species. The hybrid exhibits high activity and stability as a bifunctional catalyst for ORR and OER, attributed to the synergistic effect of a dual-carbon network, along with the enriched active sites derived from the heteroatom doping and unique metal sulfide microstructure. Excitingly, the rechargeable Zn–air battery equipped with $Co_{0.2}Fe_{0.6}S_x$-Gra/CNT as a cathode catalyst delivers a maximum power density up to 366 mW cm^{-2} and long-term charge and discharge durability at a current density of 10 mA cm^{-2}. The excellent electrocatalytic performance for oxygen confirms that the developed dual-carbon based metal sulfide catalyst can be used as a potential bifunctional catalyst for ORR and OER in the rechargeable Zn–air battery.

Experimental

Synthesis process of the $Co_{0.2}Fe_{0.6}S_x$-Gra/CNT

Thiourea (4 g), Co and Fe nitrates (0.8 g), graphene (0.03 g) and CNT (0.12 g) were added into deionized water (5 ml) to form a mixed solution. The mixture was poured into an agate jar containing ZrO$_2$ balls ($D = 5$ mm) for ball-milling at 250 rpm for 90 min, similar to our previous reported work.[58] Then, the powder contained thiourea, metal species, graphene and CNT was obtained *via* freeze drying process. The *in situ* pyrolysis process was carried out at 800 °C for 2 h with a temperature rise rate of 5 °C min^{-1}. Finally, the hybrid of dual metallic sulfides-

anchored nitrogen-doped graphene and CNT was successfully fabricated, and named as $Co_{0.2}Fe_{0.6}S_x$-Gra/CNT. To highlight the advantages of a dual-carbon network, the hybrid of the dual metallic sulfides-anchored nitrogen-doped graphene (named $Co_{0.2}Fe_{0.6}S_x$-Gra) was also prepared via similar pyrolysis under the same condition, without the addition of CNT.

Characterization

The morphology of $Co_{0.2}Fe_{0.6}S_x$-Gra/CNT and $Co_{0.2}Fe_{0.6}S_x$-Gra was determined by field-emission transmission electron microscopy (FETEM, JEM-2100F), and their elemental composition and distribution were observed by energy dispersive spectrometer (EDS). The microstructure and phase composition of the as-synthesized samples were analyzed by X-ray diffraction (XRD) and Raman spectroscopy. The chemical composition and configuration of the samples were observed by X-ray photoelectron spectroscopy (XPS, Thermo Fisher Scientific 250xi).

Electrochemical tests

The electrochemical performance of the fabricated hybrids for ORR and OER was measured by a Chenhua Instruments 760D electrochemical analyzer with a standard three-electrode setup at room temperature. A saturated calomel electrode and platinum wire electrode were chosen as the reference electrode and auxiliary electrode, respectively. A carbon (GC) rotating disk electrode (RDE, PINE, PA, USA, 0.19625 cm^2) and carbon (GC) rotating ring disk electrode (RRDE, PINE, PA, USA, 0.2475 cm^2) were separately chosen as the different working electrodes. 2.0 mg of the catalyst was dispersed in 500 μL of isopropanol and 0.1% Nafion (4 : 1) solution, and sonicated for 1 h to form a uniform catalyst ink. Both ORR and OER tests were performed in O_2-saturated 0.1 M KOH electrolyte solutions. The AC voltage for the EIS test was recorded at −0.2 V with an amplitude of 10 mV and a frequency range of 100 kHz to 0.1 Hz.

The practical electrocatalytic performance in the battery was evaluated by a home-made rechargeable Zn–air battery equipped with $Co_{0.2}Fe_{0.6}S_x$-Gra/CNT as the cathode catalyst. The polished and cleaned Zn plate (1.0 mm) and 6.0 M KOH solution were used as the anode and electrolyte, respectively. The pre-mixed catalyst ink (2.0 mg catalyst dispersed in 500 μL isopropyl alcohol and 0.5 wt% Nafion solution) was sprayed into the carbon fiber paper (Toray TGP-H-090) with a loading of 1.0 mg cm^{-2}. The polarization and power density were measured via galvanodynamic method with the current density from 0 to 1800 mA cm^{-2}. The charge and discharge durability of the Zn–air battery was tested at a current density of 10 mA cm^{-2}.

Conclusions

In summary, we have developed a facile and effective approach to fabricate a hybrid with Co/Fe sulfide nanoparticles anchored on nitrogen-doped graphene and CNT ($Co_{0.2}Fe_{0.6}S_x$-Gra/CNT). The construction of the dual carbon system endows closely combined forces between Co and Fe, along with uniformly dispersed nitrogen dopants with the feature of a relatively high ratio of pyrrolic-N species. The hybrid exhibits high activity and stability as

a bifunctional catalyst for ORR and OER, attributed to the synergistic effect of the dual-carbon network, along with the enriched active sites derived from the heteroatom doping and unique metallic sulfide microstructure. Excitingly, the rechargeable Zn–air battery equipped with $Co_{0.2}Fe_{0.6}S_x$-Gra/CNT as the cathode catalyst delivers a maximum power density up to 366 mW cm^{-2} and long-term charge and discharge durability at a current density of 10 mA cm^{-2}. The excellent electrocatalytic performance for oxygen confirms that the developed dual-carbon based metallic sulfide catalyst can be used as a potential bifunctional catalyst for ORR and OER in a rechargeable Zn–air battery.

Data availability

The data supporting this article have been included as part of the ESI.†

Author contributions

Yongxia Wang: writing – original draft, project administration, funding acquisition. Jingjing Liu: investigation, methodology. Jiaxi Liu: formal analysis. Zhaodi Wang: methodology, investigation, data curation. Biyan Zhuang: methodology, investigation. Nengneng Xu: investigation. Xiangzhi Cui: methodology, writing – review & editing. Jinli Qiao: supervision, writing – review & editing.

Conflicts of interest

There are no conflicts to declare.

Acknowledgements

Notes and references

1 M. Wu, G. Zhang, M. Wu, J. Prakash and S. Sun, *Energy Storage Mater.*, 2019, **21**, 253–286.
2 T. Szkopek, *Nat. Nanotechnol.*, 2021, **16**, 853–854.
3 N. Xu and J. Qiao, *J. Electrochem.*, 2020, **26**, 531–562.
4 J. Zhao, C. Fu, K. Ye, Z. Liang, F. Jiang, S. Shen, X. Zhao, L. Ma, Z. Shadike, X. Wang, J. Zhang and K. Jiang, *Nat. Commun.*, 2022, **13**, 685.
5 W. Lee, Y. J. Ko, J. H. Kim, C. H. Choi, K. H. Chae, H. Kim, Y. J. Hwang, B. K. Min, P. Strasser and H. S. Oh, *Nat. Commun.*, 2021, **12**, 4271.
6 G. Yasin, S. Ibrahim, S. Ajmal, S. Ibraheem, S. Ali, A. K. Nadda, G. Zhang, J. Kaur, T. Maiyalagan, R. K. Gupta and A. Kumar, *Coord. Chem. Rev.*, 2022, **469**, 214669.
7 S. Wang, X. Gao, X. Mo, D. Phillips and E. Tse, *ACS Catal.*, 2023, **13**, 5599–5608.
8 J. Zhao, Y. He, J. Wang, J. Zhang, L. Qiu, Y. Chen, C. Zhong, X. Han, Y. Deng and W. Hu, *Chem. Eng. J.*, 2022, **435**, 134261.

9 R. Zeng, Y. Yang, X. Feng, H. Li, L. Gibbs, F. DiSalvo and H. Abruña, *Sci. Adv.*, 2022, **8**, 1584.

10 Y. Ma, Y. Yu, J. Wang, J. Lipton, H. Tan, L. Zheng, T. Yang, Z. Liu and X. Loh, *Adv. Sci.*, 2022, **9**, 2105192.

11 Y. Wang, M. Wu, J. Li, H. Huang and J. Qiao, *J. Mater. Chem. A*, 2020, **8**, 19043–19049.

12 Y. Wang, J. Liu, T. Lu, R. He, N. Xu and J. Qiao, *Appl. Catal., B*, 2023, **321**, 122041.

13 H. Jiang, J. Gu, X. Zheng, M. Liu, X. Qiu, L. Wang, W. Li, Z. Chen, X. Ji and J. Li, *Energy Environ. Sci.*, 2019, **12**, 322–333.

14 Z. Pan, H. Chen, J. Yang, Y. Ma, Q. Zhang, Z. Kou, X. Ding, Y. Pang, L. Zhang, Q. Gu, C. Yan and J. Wang, *Adv. Sci.*, 2019, **6**, 1900628.

15 J. Hou, B. Zhang, Z. Li, S. Cao, Y. Sun, Y. Wu, Z. Gao and L. Sun, *ACS Catal.*, 2018, **8**, 4612–4621.

16 A. Wang, X. Zhang, S. Gao, C. Zhao, S. Kuang, S. Lu, J. Niu, G. Wang, W. Li, D. Chen, H. Zhang, X. Zhou, S. Zhang, B. Zhang and W. Wang, *Adv. Mater.*, 2022, **34**, e2204247.

17 Y. Liu, Y. Xu, H. Wang, J. Zhang, H. Zhao, L. Chen, L. Xu, Y. Xie and J. Huang, *Catalysts*, 2022, **12**, 806.

18 Q. Xiong, Y. Wang, P. Liu, L. Zheng, G. Wang, H. Yang, P. Wong, H. Zhang and H. Zhao, *Adv. Mater.*, 2018, **30**, e1801450.

19 Q. Zheng, Y. Xiong, K. Tang, M. Wu, H. Hu, T. Zhou, Y. Wu, Z. Cao, J. Sun, X. Yu and C. Wu, *Nano Energy*, 2022, **92**, 106750.

20 M. Yin, H. Miao, J. Dang, B. Chen, J. Zou, G. Chen and H. Li, *J. Power Sources*, 2022, **545**, 231902.

21 Y. Cao, X. Zheng, H. Zhang, J. Zhang, X. Han, C. Zhong, W. Hu and Y. Deng, *J. Power Sources*, 2019, **437**, 226893.

22 J. Du, R. Wang, Y. Lv, Y. Wei and S. Zang, *Chem. Commun.*, 2019, **55**, 3203–3206.

23 J. Li, T. Wan, J. Li, Z. Zhang, Y. Wang and G. Liu, *Appl. Surf. Sci.*, 2022, **575**, 151728.

24 Z. Wu, J. Wang, M. Song, G. Zhao, Y. Zhu, G. Fu and X. Liu, *ACS Appl. Mater. Interfaces*, 2018, **10**, 25415–25421.

25 M. Zhou, H. Wang and S. Guo, *Chem. Soc. Rev.*, 2016, **45**, 1273–1307.

26 H. Wang, Y. Liang, Y. Li and H. Dai, *Angew Chem. Int. Ed. Engl.*, 2011, **50**, 10969–10972.

27 X. Han, X. Wu, C. Zhong, Y. Deng, N. Zhao and W. Hu, *Nano Energy*, 2017, **31**, 541–550.

28 K. Song, Y. Feng, X. Zhou, T. Qin, X. Zou, Y. Qi, Z. Chen, J. Rao, Z. Wang, N. Yue, X. Ge, W. Zhang and W. Zheng, *Appl. Catal., B*, 2022, **316**, 121591.

29 T. Xing, L. Li, L. Hou, X. Hu, S. Zhou, R. Peter, M. Petravic and Y. Chen, *Carbon*, 2013, **57**, 515–519.

30 T. Wu, Y. Lin and C. Liao, *Carbon*, 2005, **43**, 734–740.

31 L. Zhang, L. Liu, J. Feng and A. Wang, *J. Colloid Interface Sci.*, 2024, **661**, 102–112.

32 D. Wu, M. Haq, L. Zhang, J. Feng, F. Yang and A. Wang, *J. Colloid Interface Sci.*, 2024, **662**, 149–159.

33 M. Haq, D. Wu, Z. Ajmal, Q. Ruan, S. Khan, L. Zhang, A. Wang and J. Feng, *Appl. Catal., B*, 2024, **344**, 123632.

34 J. Cai, H. Liu, Y. Luo, Y. Xiong, L. Zhang, S. Wang, K. Xiao and Z.-Q. Liu, *J. Energy Chem.*, 2022, **74**, 420–428.

35 X. Zheng, Y. Cao, Z. Wu, W. Ding, T. Xue, J. Wang, Z. Chen, X. Han, Y. Deng and W. Hu, *Adv. Energy Mater.*, 2022, **12**, 2103275.

36 Z. Sheng, L. Shao, J. Chen, W. Bao, F. Wang and X. Xia, *ACS Nano*, 2011, **5**, 4350–4358.

37 Y. Zhang, H. Fu, C. He, H. Zhang, Y. Li, G. Yang, Y. Cao, H. Wang, F. Peng, X. Yang and H. Yu, *J. Phys. Chem. Lett.*, 2022, **13**, 6187–6193.

38 N. Solati, M. Çankaya, A. Kahraman, K. Şimşek, C. Titus, S. Lee, D. Nordlund, H. Ogasawara, A. Tekin and S. Kaya, *Today Energy*, 2023, **35**, 101323.

39 B. Wu, H. Meng, D. M. Morales, F. Zeng, J. Zhu, B. Wang, M. Risch, Z. Xu and T. Petit, *Adv. Funct. Mater.*, 2022, **32**, 2204137.

40 H. Yang, J. Miao, S. Hung, J. Chen, H. Tao, X. Wang, L. Zhang, R. Chen, J. Gao, H. Chen, L. Dai and B. Liu, *Sci. Adv.*, 2016, **2**, e1501122.

41 S. Huang, Y. Meng, Y. Cao, S. He, X. Li, S. Tong and M. Wu, *Appl. Catal., B*, 2019, **248**, 239–248.

42 Q. Lv, W. Si, J. He, L. Sun, C. Zhang, N. Wang, Z. Yang, X. Li, X. Wang, W. Deng, Y. Long, C. Huang and Y. Li, *Nat. Commun.*, 2018, **9**, 3376.

43 R. Zhang, S. Cheng, N. W. Li and N. Ke, *Appl. Surf. Sci.*, 2020, **503**, 144146.

44 L. Peng, Y. Wang, I. Masood, B. Zhou, Y. Wang, J. Lin, J. Qiao and F.-Y. Zhang, *Appl. Catal., B*, 2020, **264**, 118447.

45 Y. Lin, P. Teng, C. Yeh, M. Koshino, P. Chiu and K. Suenaga, *Nano Lett.*, 2015, **15**, 7408–7413.

46 J. Duan, S. Chen, M. Jaroniec and S. Z. Qiao, *ACS Catal.*, 2015, **5**, 5207–5234.

47 Q. Wang, Y. Lei, Y. Zhu, H. Wang, J. Feng, G. Ma, Y. Wang, Y. Li, B. Nan, Q. Feng, Z. Lu and H. Yu, *ACS Appl. Mater. Interfaces*, 2018, **10**, 29448–29456.

48 J. Zhang, X. Bai, T. Wang, W. Xiao, P. Xi, J. Wang, D. Gao and J. Wang, *Nanomicro Lett.*, 2019, **11**, 2.

49 S. Chen, W. Liang, X. Wang, Y. Zhao, S. Wang, Z. Li, S. Wang, L. Hou, Y. Jiang and F.-J. Gao, *J. Alloys Compd.*, 2023, **931**, 167575.

50 J. Li, H. Xue, N. Xu, X. Zhang, Y. Wang, R. He, H. Huang and J. Qiao, *Mater. Rep.: Energy*, 2022, **2**, 100090.

51 H. Yang, B. Wang, H. Li, B. Ni, K. Wang, Q. Zhang and X. Wang, *Adv. Energy Mater.*, 2018, **8**, 1801839.

52 H. Zhang, X. Wang, Z. Yang, S. Yan, C. Zhang and S. Liu, *ACS Sustain. Chem. Eng.*, 2019, **8**, 1004–1014.

53 Z. Cai, I. Yamada and S. Yagi, *ACS Appl. Mater. Interfaces*, 2020, **12**, 5847–5856.

54 J. Wang, H. Lu, Q. Hong, Y. Cao, X. Li and J. Bai, *Chem. Eng. J.*, 2017, **330**, 1342–1350.

55 R. Wang, J. Liu, J. Xie, Z. Cai, Y. Yu, Z. Zhang, X. Meng, C. Wang, X. Xu and J. Zou, *Appl. Catal., B*, 2023, **324**, 122230.

56 W. Fang, H. Hu, T. Jiang, G. Li and M. Wu, *Carbon*, 2019, **146**, 476–485.

57 Y. Wang, N. Xu, R. He, L. Peng, D. Cai and J. Qiao, *Appl. Catal., B*, 2021, **285**, 119811.

58 I. Jeon, H. Choi, S. Jung, J. Seo, M. Kim, L. Dai and J. Baek, *J. Am. Chem. Soc.*, 2012, **135**, 1386–1393.